

# The $B \rightarrow X_s \gamma \gamma$ decay in the standard model and the general two-Higgs-doublet model

Junjie Cao

Department of Physics, Henan Normal University, Xinxiang, Henan, 453002, People's Republic of China

Zhenjun Xiao

CCAST(World Laboratory), P.O.Box 8730, Beijing 100080, People's Republic of China

Department of Physics, Henan Normal University, Xinxiang, Henan, 453002, People's Republic of China

Department of Physics, Peking University, Beijing, 100871, People's Republic of China

Gongru Lu

CCAST(World Laboratory), P.O.Box 8730, Beijing 100080, People's Republic of China

Department of Physics, Henan Normal University, Xinxiang, Henan, 453002, People's Republic of China

(November 4, 2018)

## Abstract

Based on the low-energy effective Hamiltonian, we calculate the new physics corrections to the branching ratio and the differential distributions of the rare decay  $B \rightarrow X_s \gamma \gamma$  induced by the new gluonic and electroweak charged-Higgs penguin diagrams in the general two-Higgs-doublet model with the restriction  $\lambda_{ij}^{U,D} = 0$  for  $i \neq j$ . Within the considered parameter space, we see the following: (a) the standard model predictions of  $\mathcal{B}(B \rightarrow X_s \gamma \gamma)$  and  $A_{FB}$  have a moderate  $m_s$  dependence; (b) in model III, the prediction of the branching ratio  $\mathcal{B}(B \rightarrow X_s \gamma \gamma)$  ranges from one third to three times of the standard model prediction, but is highly correlated with that of  $\mathcal{B}(B \rightarrow X_s \gamma)$ ; (c) the new physics enhancement to the branching ratio  $\mathcal{B}(B \rightarrow X_s \gamma \gamma)$  in model II can be as large as  $(30 - 50)\%$ ; (d) the contribution from 1PR diagrams is dominant and hence four normalized differential distributions are insensitive to the variation of scale  $\mu$  and possible new physics corrections; (e) due to the smallness of its decay rate and the long-distance background, the  $B \rightarrow X_s \gamma \gamma$  decay is not a better process in detecting new physics than the  $B \rightarrow X_s \gamma$  decay.

PACS numbers: 13.25.Hw, 12.15.Ji, 12.40.Bx, 12.60.Fr

## I. INTRODUCTION

The flavor changing neutral current (FCNC) inclusive transition  $B \rightarrow X_s \gamma$  has been a subject of great interest during the past few years. The basic theoretical framework is the standard model (SM) at scales  $m_w$  or  $m_t$ . QCD short distance corrections [1] are then incorporated via the renormalization group technique to yield the low energy effective Hamiltonian valid at scale  $O(m_b)$  which is relevant for B decay processes [2,3].

As is well known, the rare decay  $B \rightarrow X_s \gamma$  is theoretically very clear, measured at CLEO [4,5] with increasing accuracy and in remarkable agreement with theoretical estimates. Great progress in both the theoretical calculation [6] and the experimental measurement [5] for  $B \rightarrow X_s \gamma$  decay enable one to constrain the new physics models, such as the two-Higgs-doublet model (2HDM) [7], the minimal supersymmetric standard model (MSSM) [8] and the Technicolor models [9]. In light of these developments, it is natural to consider other inclusive channels which as a whole may separate out contributions from various operators in the effective Hamiltonian.

The rare flavor changing neutral current inclusive transition  $B \rightarrow X_s \gamma \gamma$ , which is expected to be  $\sim 10^{-3}$  smaller in its branching ratio relative to  $B \rightarrow X_s \gamma$ , has attracted new attention in view of the planned experiments at KEK and SLAC B-factories and existing accelerators, which may test branching ratios as low as  $10^{-8}$ . Just like the decay  $B \rightarrow X_s \gamma$ , the decay  $B \rightarrow X_s \gamma \gamma$  is relatively clean after some proper precaution to take out effects due to strong resonance, for instance, the effect of  $\eta_c$  at its peak to the two photon spectrum [10]. The studies about these rare decay modes will then provide further opportunities in testing the whole technology of weak decays, or better yet in providing some clues of new physics.

There have been some theoretical investigations for the process  $B \rightarrow X_s \gamma \gamma$ , which corresponds at the quark level to the transition  $b \rightarrow s \gamma \gamma$ . Theoretical calculations in the SM were firstly done on the basis of pure electroweak theory [11,12] and subsequently improved to include the leading order (LO) QCD effects [13,14]. Nearly all the studies of  $B \rightarrow X_s \gamma \gamma$  and  $B \rightarrow X_s \gamma$  decays are based on the free decay of  $b$  quark and can be justified from the heavy quark effective theory (HQET). According to the argument in Ref. [15], the HQET corrections to these rare decay modes are strongly suppressed by powers of  $(\Lambda/m_b)^2$ . Furthermore, Choudhury and Yao [16] have shown that even when  $(\Lambda/m_c)^2$  and  $(\Lambda/m_c)^4$  corrections are included, the overall HQET corrections to the free quark results of  $B \rightarrow X_s \gamma \gamma$  are only a few percent and can be safely neglected. In this paper, we will present our results at free quark level.

Recently, we estimated the new physics contributions to the inclusive decay  $b \rightarrow q g^* \rightarrow q \bar{q}' q'$  with  $q \in \{d, s\}$  and  $q' \in \{u, d, s\}$  in the model III: the third-type two-Higgs-doublet model [17,18], and found that the new physics contributions can be significant [19]. In this paper, we calculate the new physics corrections to the branching ratio and differential distributions of the rare decay  $B \rightarrow X_s \gamma \gamma$  induced by the new gluonic and electroweak charged-Higgs penguin diagrams in the model III.

The plan of this paper is as follows: in the next section, we give a brief review of the process  $B \rightarrow X_s \gamma \gamma$  in the SM at LO approximation, present the relevant formulae and discuss some general characteristics of this process. In Sec. III, we will investigate in detail this rare decay in the model III and present some numerical results. In the last section,

concluding remarks are added.

## II. $B \rightarrow X_S \gamma \gamma$ IN THE SM

By the use of an extension of Low's low energy theorem [13,20], or alternatively, by applying the equation of motions [21], the most general effective Hamiltonian that describes radiative  $b \rightarrow s$  decays with up to three emitted gluons or photons is given by <sup>1</sup>

$$H_{eff} = -\frac{4G_F}{\sqrt{2}} V_{tb} V_{ts}^* \sum_{i=1}^8 C_i(\mu) O_i, \quad (1)$$

where the current-current, penguin, electroweak- and chromo-magnetic dipole operators are of the form

$$\begin{aligned} O_1 &= (\bar{s}_\alpha \gamma^\mu L c_\beta) (\bar{c}_\beta \gamma_\mu L b_\alpha), \\ O_2 &= (\bar{s}_\alpha \gamma^\mu L c_\alpha) (\bar{c}_\beta \gamma_\mu L b_\beta), \\ O_3 &= (\bar{s}_\alpha \gamma^\mu L b_\alpha) \sum_{q=u \cdots b} (\bar{q}_\beta \gamma_\mu L q_\beta), \\ O_4 &= (\bar{s}_\alpha \gamma^\mu L b_\beta) \sum_{q=u \cdots b} (\bar{q}_\beta \gamma_\mu L q_\alpha), \\ O_5 &= (\bar{s}_\alpha \gamma^\mu L b_\alpha) \sum_{q=u \cdots b} (\bar{q}_\beta \gamma_\mu R q_\beta), \\ O_6 &= (\bar{s}_\alpha \gamma^\mu L b_\beta) \sum_{q=u \cdots b} (\bar{q}_\beta \gamma_\mu R q_\alpha), \\ O_7 &= \frac{e}{16\pi^2} \bar{s}_\alpha \sigma^{\mu\nu} (m_b R + m_s L) b_\alpha F_{\mu\nu}, \\ O_8 &= \frac{g_s}{16\pi^2} \bar{s}_\alpha \sigma^{\mu\nu} (m_b R + m_s L) \lambda_{\alpha\beta}^a b_\beta G_{\mu\nu}^a. \end{aligned} \quad (2)$$

where  $\alpha$  and  $\beta$  are color indices,  $a=1, \dots, 8$  labels  $SU(3)_C$  generators, and  $L, R=(1 \mp \gamma_5)/2$ , while  $F_{\mu\nu}$  and  $G_{\mu\nu}^a$  denote the QED and QCD field strength tensors, respectively.

The Wilson coefficients  $C_i(\mu)$  in Eq.(1) are process independent and their renormalization is determined only by the basis of operators  $O_i$ . In our calculation of the leading order matrix elements of  $b \rightarrow s \gamma \gamma$  shown in Fig.1, we find no regulation scheme dependence enters through the new class of penguin diagrams with two external photon. This means that it is suffice to use LO regularization-scheme-independent Wilson coefficients  $C_{1,\dots,6}$ ,  $C_{7\gamma}$  and  $C_{8g}$  [22] and we need not consider the matrix elements due to the insertion of  $O_5$  and  $O_6$  into the one-photon penguin diagrams. In Table I, we present the numerical values of the Wilson coefficients at the scale  $\mu = O(m_b)$  <sup>2</sup>.

---

<sup>1</sup>Strictly speaking, operators  $(\bar{s}_\alpha \gamma^\mu L u_\alpha)(\bar{u}_\beta \gamma_\mu L b_\beta)$  and  $(\bar{s}_\alpha \gamma^\mu L u_\beta)(\bar{u}_\beta \gamma_\mu L b_\alpha)$  should be added. Here we neglect them for their small coefficients.

<sup>2</sup> These Wilson coefficients are numerically well consistent with those given in Ref. [14].

At the leading order, the amplitude for the decay  $b(p) \rightarrow s(p') + \gamma(k_1) + \gamma(k_2)$  can be expressed as [14]

$$A = -\frac{i e^2 G_F}{\sqrt{2} \pi^2} V_{tb} V_{ts}^* \bar{u}_s(p') \cdot \left[ F_2 W_2^{\mu\nu} + F_5 (m_b W_{5,b}^{\mu\nu} R + m_s W_{5,s}^{\mu\nu} L) + F_7 W_7^{\mu\nu} \right] u_b(p) \epsilon_\mu(k_1) \epsilon_\nu(k_2) , \quad (3)$$

with

$$\begin{aligned} F_2 = & [N_c C_1(\mu) + C_2(\mu)] Q_u^2 \kappa_c \\ & + C_3(\mu) \left\{ N_c \left[ Q_d^2 (\kappa_d + \kappa_s + \kappa_b) + Q_u^2 (\kappa_u + \kappa_c) \right] + Q_d^2 (\kappa_s + \kappa_b) \right\} \\ & + C_4(\mu) \left\{ Q_d^2 \left[ (\kappa_d + \kappa_s + \kappa_b) + Q_u^2 (\kappa_u + \kappa_c) \right] + N_c Q_d^2 (\kappa_s + \kappa_b) \right\} \\ & - [N_c C_5(\mu) + C_6(\mu)] \left[ Q_d^2 (\kappa_d + \kappa_s + \kappa_b) + Q_u^2 (\kappa_u + \kappa_c) \right] , \end{aligned} \quad (4)$$

$$F_5 = [C_5(\mu) + N_c C_6(\mu)] Q_d^2 , \quad (5)$$

$$F_7 = C_7(\mu) Q_d , \quad (6)$$

$$W_2^{\mu\nu} = -i \left\{ \frac{1}{k_1 \cdot k_2} \left[ k_1^\nu \epsilon_{\mu\rho\sigma\lambda} \gamma^\rho k_1^\sigma k_2^\lambda - k_2^\mu \epsilon_{\nu\rho\sigma\lambda} \gamma^\rho k_1^\sigma k_2^\lambda \right] + \epsilon_{\mu\nu\rho\lambda} \gamma^\rho (k_2 - k_1)^\lambda \right\} L , \quad (7)$$

$$W_{5,q}^{\mu\nu} = \frac{1}{m_q^2} \left( -i \epsilon_{\mu\nu\lambda\sigma} k_1^\lambda k_2^\sigma \gamma_5 + k_1 \cdot k_2 g^{\mu\nu} - k_1^\nu k_2^\mu \right) (1 - 2\kappa_q) + 4 \left( g^{\mu\nu} - \frac{k_1^\nu k_2^\mu}{k_1 \cdot k_2} \right) \kappa_q , \quad (8)$$

$$\begin{aligned} W_7^{\mu\nu} = & \frac{1}{2} \left[ -\frac{1}{2p \cdot k_2} \not{k}_1 \gamma^\mu (m_b R + m_s L) (\not{p} - \not{k}_2 + m_b) \gamma^\nu \right. \\ & \left. + \frac{1}{2p' \cdot k_2} \gamma^\nu (\not{p} - \not{k}_1 + m_s) \not{k}_1 \gamma^\mu (m_b R + m_s L) \right] , \end{aligned} \quad (9)$$

where  $k_1$  and  $k_2$  are four-momenta of the emitted photons,  $N_c = 3$  denotes the number of colors,  $Q_u = 2/3$  and  $Q_d = -1/3$  are the up-type and down-type quark electric charges, and the factor  $\kappa_q$  is defined as

$$\begin{aligned} \kappa_q = & \frac{1}{2} + \frac{1}{z_q} \int_0^1 \frac{dx}{x} \ln(1 - z_q x + z_q^2 x^2) \\ = & \begin{cases} \frac{1}{2} - \frac{2}{z_q} \left( \arctan \sqrt{\frac{z_q}{4-z_q}} \right)^2 & \text{if } z_q < 4 , \\ \frac{1}{2} + \frac{1}{z_q} \left[ -\frac{\pi^2}{2} + 2 \left( \ln \frac{\sqrt{z_q} + \sqrt{z_q - 4}}{2} \right)^2 - 2i\pi \ln \left( \frac{\sqrt{z_q} + \sqrt{z_q - 4}}{2} \right) \right] & \text{otherwise .} \end{cases} \end{aligned} \quad (10)$$

Here  $z_q = 2k_1 \cdot k_2 / m_q^2$ . The masses appearing in  $W_7^{\mu\nu}$  arise from operator  $O_7$  while those in  $W_{5,q}^{\mu\nu}$  are internal quark masses in the loops (see Fig.1). In our numerical analysis, we take all these quark masses as current mass. The factor  $\kappa_q$  in Eq.(10) is the loop integral function [23] and its absorption part reflects intermediate quark threshold effect. In getting the expressions of  $W_i^{\mu\nu}$  that are essential to obtain the matrix elements of  $b \rightarrow s \gamma \gamma$  decay presented in [13], we used the following identities:

$$\gamma_\mu \gamma_\lambda \gamma_\sigma = g_{\sigma\lambda} \gamma_\mu + g_{\mu\lambda} \gamma_\sigma - g_{\mu\sigma} \gamma_\lambda + i \epsilon_{\mu\rho\sigma\lambda} \gamma^\rho \gamma_5 , \quad (11)$$

$$\begin{aligned} \gamma_{\mu_1} \gamma_{\mu_2} \gamma_{\mu_3} \gamma_{\mu_4} = & i \epsilon_{\mu_1 \mu_2 \mu_3 \mu_4} \gamma_5 - g_{\mu_3 \mu_4} g_{\mu_1 \mu_2} + g_{\mu_2 \mu_4} g_{\mu_1 \mu_3} - g_{\mu_2 \mu_3} g_{\mu_1 \mu_4} + g_{\mu_3 \mu_4} \gamma_{\mu_1} \gamma_{\mu_2} \\ & - g_{\mu_2 \mu_4} \gamma_{\mu_1} \gamma_{\mu_3} + g_{\mu_2 \mu_3} \gamma_{\mu_1} \gamma_{\mu_4} + g_{\mu_1 \mu_4} \gamma_{\mu_2} \gamma_{\mu_3} - g_{\mu_1 \mu_3} \gamma_{\mu_2} \gamma_{\mu_4} + g_{\mu_1 \mu_2} \gamma_{\mu_3} \gamma_{\mu_4} . \end{aligned} \quad (12)$$

The square amplitude summed over spins and polarizations is then given by

$$|A|^2 = \frac{1}{4} \left( \frac{e^2 G_F}{\sqrt{2} \pi^2} V_{tb} V_{ts}^* \right)^2 m_b^4 \left\{ |F_2|^2 A_{22} + |F_5|^2 A_{55} + |F_7|^2 A_{77} + 2Re[F_7 F_2^*] A_{27} \right. \\ \left. + 2Re[F_5 F_2^* (1 - 2\kappa_s)] A_{25}^s + 2Re[F_7 F_5^*] A_{57} + 2Re[F_5 F_2^* (1 - 2\kappa_b)] A_{25}^b \right\} , \quad (13)$$

where the quantities  $A_{ij}$  denote the contractions between the tensor  $W_i^{\mu\nu*}$  and  $W_j^{\mu\nu}$ , and the first two terms and the third term of  $|A|^2$  arise from one-particle irreducible (1PI) diagrams and one-particle reducible (1PR) diagrams, respectively. In order to give the explicit expressions of  $A_{ij}$ , we introduced the following notations,

$$s = \frac{2k_1 \cdot k_2}{m_b^2}, \quad t = \frac{2p \cdot k_2}{m_b^2}, \quad u = \frac{2p \cdot k_1}{m_b^2}, \quad rho_1 = \frac{m_s^2}{m_b^2}, \\ \rho = 1 - u - t + s = \frac{p'^2}{m_b^2}, \quad \bar{s} = \frac{s}{1 - \rho}, \quad \bar{t} = \frac{t}{1 - \rho}, \quad \bar{u} = \frac{u}{1 - \rho}, \quad (14)$$

where  $m_s$  is  $s$  quark mass appearing in  $W_{5,7}^{\mu\nu}$  and  $p'$  is the momentum of the outgoing  $s$  quark. In this framework, coefficients  $A_{ij}$  are then given by

$$A_{22} = 2[(1 - \rho)^2 - (1 + \rho)s], \quad (15)$$

$$A_{55} = \left\{ 16|\kappa_b|^2 + |(1 - 2\kappa_b)s + 4\kappa_b|^2 + \rho_1[16|\kappa_s|^2 + |(1 - 2\kappa_s)\frac{s}{\rho_1} + 4\kappa_s|^2] \right\} (1 - s + \rho) \\ + 16Re \{ 8\rho_1 \kappa_b \kappa_s^* + s[\kappa_b - 2(1 + \rho_1)\kappa_b \kappa_s^* + \rho_1 \kappa_s^*] \} , \quad (16)$$

$$A_{25}^{b,s} = \pm s(1 - \rho \mp s), \quad (17)$$

$$A_{27} = - \left[ 2(1 + \rho_1)s + \frac{(\rho + \rho_1)s^2 + 2(\rho_1 - \rho)ts}{t(s - t)} + \frac{(\rho + \rho_1)s^2 + 2(\rho_1 - \rho)us}{u(s - u)} \right], \quad (18)$$

$$A_{57} = Re \left\{ 8(\kappa_b + \rho_1 \kappa_s)s - [4\rho_1(\kappa_b + \kappa_s) + s[(1 - 2\kappa_s) + \rho_1(1 - 2\kappa_b)]] \right. \\ \left. \times \left[ \frac{s^2}{t(s - t)} + \frac{s^2}{u(s - u)} \right] - 4 \left[ (\kappa_b + \rho_1 \kappa_s)(\rho - \rho_1) \left( \frac{s^2}{t(s - t)} + \frac{s^2}{u(s - u)} \right) \right] \right\} , \quad (19)$$

$$A_{77} = (1 + \rho_1) \left[ (1 - \rho)A_{77}^1 + A_{77}^2 \right] + A_{77}^3, \quad (20)$$

$$A_{77}^1 = \frac{1}{\bar{t}} \left[ 1 + \bar{u} + \frac{2\bar{u}(\bar{u} - 2)}{(1 - \bar{u})}\bar{t} + \frac{2\bar{u} - 1}{1 - \bar{u}}\bar{t}^2 \right] + (\bar{t} \leftrightarrow \bar{u}), \quad (21)$$

$$A_{77}^2 = \frac{-2}{\bar{t}^2} \left[ 1 - \frac{1 + \rho_1}{1 - \bar{u}}\bar{t} + \frac{\rho_1}{(1 - \bar{u})^2}\bar{t}^2 \right] \\ + (\rho_1 - \rho) \left( \frac{2\bar{s}}{\bar{t}(1 - \bar{u})} - \frac{\bar{s}\bar{u}}{(1 - \bar{u})^2} - \frac{\bar{u}^2}{(1 - \bar{u})^2} \right) + (\bar{t} \leftrightarrow \bar{u}), \quad (22)$$

$$A_{77}^3 = -2\frac{s}{\bar{t}\bar{u}}t \left\{ (1 + \rho_1)(2 + \bar{u}\bar{t}) + \frac{\rho_1}{1 - \rho} \left[ 1 - \frac{2(1 + \rho_1) - \bar{t}\bar{u}}{(1 - \bar{t})(1 - \bar{u})} \right] \bar{s} \right\} \\ + \frac{2s}{tu}(\rho_1 - \rho) \frac{-(1 + \rho_1)(2s + \bar{s}) - \rho_1(\bar{s}^2 - 2\bar{t}\bar{u}) + 2(2 - \rho)(1 + \rho_1)\bar{t}\bar{u}}{(1 - \bar{u})(1 - \bar{t})}, \quad (23)$$

Unlike Ref. [14], we here distinguish different  $s$  quark contributions which enter in the amplitude via  $\rho$  and  $\rho_1$  respectively. This is crucial to our results, as described below. Note

that in the  $A_{77}$  term of the square amplitude, there exists infrared (IR) divergence when one integrates the amplitude over the physical phase space. This divergence can be canceled out when one considers  $O(\alpha_e)$  virtual corrections to the  $b \rightarrow s\gamma$  amplitude [24]. In order to calculate the physical rate of interest that is free of divergence, we have to impose a cut on the energy of each photon, which will naturally correspond to the experimental cut imposed on the minimum energy of detectable photons.

In numerical calculations, we use the input parameters listed in Table II and take the following cuts:

$$E_\gamma > 100 \text{ MeV} , \quad E_s > 600 \text{ MeV} , \quad \theta > \frac{\pi}{9} , \quad (24)$$

where  $E_\gamma$  and  $E_s$  denote the energy of photon and that of the outgoing mesons respectively, and  $\theta$  is the angle between any two outgoing particles. The first constraint is required to avoid IR divergence while the last constraint is to exclude photons that are emitted too close to each other or to the outgoing  $s$  quark. For the mass of  $s$  quark, care must be taken. In principle, constituent mass should be used in the phase space integration, while the masses appeared in  $W_7^{\mu\nu}$  and  $W_5^{\mu\nu}$  should be the current mass. This means that  $\rho$  and  $\rho_1$  appeared in Eqs.(15-23) should be

$$\rho = \frac{m_s^2 (\text{constituent})}{m_b^2} \simeq \frac{m_K^2}{m_b^2} , \quad \rho_1 = \frac{m_s^2 (\text{current})}{m_b^2} . \quad (25)$$

Following Ref. [25], the branching ratio of  $B \rightarrow X_s \gamma \gamma$  decay can be written as

$$\mathcal{B}(B \rightarrow X_s \gamma \gamma) \simeq \left[ \frac{\Gamma(b \rightarrow s \gamma \gamma)}{\Gamma(b \rightarrow c l \nu_l)} \right]^{th} \times \mathcal{B}(B \rightarrow X_c l \nu_l)^{expt} . \quad (26)$$

Using the input parameters presented in Table II, setting  $\mu = m_b$  and taking the cuts given in Eq.(24), we find numerically that

$$\mathcal{B}(B \rightarrow X_s \gamma \gamma) \approx 4.6 \times 10^{-7} , \quad A_{FB}(B \rightarrow X_s \gamma \gamma) = 0.79 , \quad (27)$$

where  $A_{FB}$  is the forward-backward asymmetry of the  $B \rightarrow X_s \gamma \gamma$  decay.

If we use a common  $s$  quark mass  $m_s = 0.5 \text{ GeV}$  in the numerical calculations as Ref. [14] did, we find that

$$\mathcal{B}(B \rightarrow X_s \gamma \gamma) = 3.8 \times 10^{-7} , \quad A_{FB}(B \rightarrow X_s \gamma \gamma) = 0.76 , \quad (28)$$

which agree well with the results presented in Ref. [14], where  $\mathcal{B}(B \rightarrow X_s \gamma \gamma) = 3.7 \times 10^{-7}$  and  $A_{FB} = 0.78$ . For  $m_s = 0.15 \text{ GeV}$ , however, we find that

$$\mathcal{B}(B \rightarrow X_s \gamma \gamma) = 5.1 \times 10^{-7} , \quad A_{FB}(B \rightarrow X_s \gamma \gamma) = 0.81 . \quad (29)$$

From above numerical results, we find that the  $m_s$ -dependence is weak for  $A_{FB}$ , but relatively strong for the branching ratio.

Among all the contributions to the decay rate, the contribution from 1PR diagrams is predominant, larger than 97% of the total, which is due to the cancellation between  $C_1$  and  $C_2$  and the QCD enhancement of  $|C_7|$ . Numerical results also show that the branching ratio

is sensitive to the cuts we have imposed. For example, if we demand  $\theta$  in Eq.(24) larger than  $\pi/6$ , the branching ratio will reduce to  $3.6 \times 10^{-7}$ . Moreover, because of the scale dependence of Wilson coefficients, there exists a  $\sim 25\%$  theoretical uncertainty at leading order approximation, as is the case for  $B \rightarrow X_s \gamma$ .

In Fig.2, we present the normalized differential distribution  $(1/\Gamma)d\Gamma/ds$  versus  $s$  ( solid curve ). Comparing with the corresponding result given in [12], we find that the peak due to  $c\bar{c}$  threshold effect is smeared and the average invariant mass of the two photons is lowered when QCD corrections are added. In Figs.(3-5) , the normalized differential distribution  $(1/\Gamma)d\Gamma/d\cos\theta_{\gamma\gamma}$  versus  $\cos\theta_{\gamma\gamma}$  (solid curve in Fig.3) and the spectrum of the two photons, defined as the photon with lower energy (solid curve in Fig.4) and the photon with higher energy (solid curve in Fig.5), are plotted.

From these four figures, one can understand the kinematics of the process as follows: *an energetic  $s$  quark with mean energy around 2.0GeV tends to be emitted, compensated by the harder of the two photons; while the less energetic photon tends to go in the direction of the  $s$  quark. This topology is typical of a bremsstrahlung event of the  $s$  quark.* Such kinematics are very useful for us to separate the short-distance (SD) signal from the long-distance (LD) background, which may come from the channel  $B \rightarrow X_s \eta (\eta') \rightarrow X_s \gamma\gamma$  [10,12]. For example, by demanding  $s \leq 0.3$  and  $\cos\theta_{\gamma\gamma} \leq 0$ , about 75% of the signal is remained while almost all the LD background are removed.

In Figs.(2-5), the contribution from 1PI diagrams (dashed curve) and that from the interference between 1PI and 1PR (dot-dashed curve) are also plotted. From these figures, we can see that except in some marginal area, the contributions from 1PI diagrams and the interference are much smaller than those coming from 1PR diagrams. Taking this in mind, one can infer that though the four normalized differential distributions are calculated at leading order approximation, they are insensitive to the variation of scale. The reason is that, to a good approximation, a common factor  $|C_7(\mu)|^2$  can be extracted from both  $\Gamma$  and  $d\Gamma$  and will disappear in the ratio of them. This feature becomes more evident when the cuts of  $s \leq 0.3$  and  $\cos\theta_{\gamma\gamma} \leq 0$  are imposed, which removes nearly all the contributions of  $O_1 \sim O_6$  (see Fig.2). In fact, a more general statement is that: as long as the new physics effects beyond the SM appear only in the matching of the Wilson coefficients of the standard effective operator basis, which is so in the MSSM [25], and  $|C_7|$  is not suppressed as required by  $b \rightarrow s\gamma$ , these four observable distributions are insensitive to the variation of scale  $\mu$  and the new physics.

### III. $B \rightarrow X_s \gamma\gamma$ IN MODEL III

#### A. Model description

The two-Higgs-doublet model (2HDM) [7] is the simplest extension of the SM . During past years, the models I and II have been studied extensively in literature and tested experimentally and the model II has been very popular since it is the building block of the MSSM. In Ref. [12], the authors studied the  $B \rightarrow X_s \gamma\gamma$  decay in the SM and models I and II in the basis of pure electroweak theory [11], and found that the branching ratios in models I and II can be appreciably different from that in the SM [12]. In this paper, we focus on estimating the new physics effects on the  $B \rightarrow X_s \gamma\gamma$  decay in the framework of the third

type of 2HDM, usually known as the model III [18]. In the model III, no discrete symmetry is imposed and both up- and down-type quarks may couple with either of the two Higgs doublets. The Yukawa coupling in quark sector in this case is [18]

$$\mathcal{L}_Y = \eta_{ij}^U \bar{Q}_{iL} \tilde{\phi}_1 U_{jR} + \eta_{ij}^D \bar{Q}_{iL} \tilde{\phi}_1 D_{jR} + \xi_{ij}^U \bar{Q}_{iL} \tilde{\phi}_2 U_{jR} + \xi_{ij}^D \bar{Q}_{iL} \tilde{\phi}_2 D_{jR} + h.c. , \quad (30)$$

where  $\phi_1$  and  $\phi_2$  are the two Higgs doublets and  $\eta_{ij}^{U,D}$  and  $\xi_{ij}^{U,D}$  are the Yukawa couplings. As described in [18], in order to let  $\phi_1$  correspond to generate fermion masses while  $\phi_2$  to introduce new interactions, one can choose the following parameterization of the Higgs doublets

$$\phi_1 = \frac{1}{\sqrt{2}} \left[ \begin{pmatrix} 0 \\ v + H^0 \end{pmatrix} + \begin{pmatrix} \sqrt{2}\chi^+ \\ i\chi^0 \end{pmatrix} \right] , \quad \phi_2 = \frac{1}{\sqrt{2}} \begin{pmatrix} \sqrt{2}H^+ \\ H^1 + iH^2 \end{pmatrix} , \quad (31)$$

where  $v = (\sqrt{2}G_F)^{-1/2} = 246\text{GeV}$ . After the rotation that diagonalizes the mass matrices of quark fields and that of the Higgs doublets, we can get the Lagrangian that is relevant for our following discussions. The main features of model III are as follows [18]:

- FCNC may exist at the tree level. The neutral and the charged flavor changing couplings are related by:

$$\xi_{charge}^U = \xi_{neutral}^U V_{CKM} , \quad \xi_{charge}^D = V_{CKM} \xi_{neutral}^D , \quad (32)$$

where  $V_{CKM}$  is the ordinary mixing matrix between down-type quarks [26], and

$$\xi_{neutral}^{U,D} = (V_L^{U,D})^{-1} \xi^{U,D} V_R^{U,D} . \quad (33)$$

- Like the models I and II, there are also five Higgs bosons in model III: the light and heavy CP-even neutral Higgs boson  $h^0$  and  $\bar{H}^0$ , one CP-odd neutral Higgs boson  $A^0$  and a pair of charged Higgs bosons  $H^\pm$ . The transformation relation between  $(H^0, H^1, H^2)$  in Eq.(31) and the mass eigenstates  $(\bar{H}^0, h^0, A^0)$  can be found in [18].

In the following of this paper, we will parameterize  $\xi_{neutral}^{U,D}$  as Ref. [18]

$$(\xi_{neutral}^{U,D})_{ij} = \lambda_{ij}^{U,D} \frac{\sqrt{m_i m_j}}{v} , \quad (34)$$

and treat  $\lambda_{ij}^{U,D}$  as basic free parameters.

## B. Experimental constraints

There is a considerable interest in the constraint of the parameter space of the 2HDM, especially in model III, since the FCNC may appear at the tree level. Compared with the SM, the additional free parameters of model III are the masses of the additional Higgs bosons and the coupling constants  $\lambda_{ij}$ . In this subsection, we summarize the main constraints on these parameters from direct searches at LEP experiments [27], and from the measurements of  $F^0 - \bar{F}^0$  mixing with  $F^0 = K^0, B_d^0$ .



Let's firstly turn to mass constraints. The LEP Working Group for Higgs boson searches [28] has recently reported excess of events that might be due to the production of a neutral Higgs boson weighing about 115 GeV, and placed a lower mass limit for the SM Higgs boson  $M_{H^0} > 113.5$  GeV at 95%*C.L.*. For the  $h^0$  and  $A^0$  Higgs bosons of the MSSM, the new 95%*C.L.* limit [29] is  $M_{h^0} > 88.3$  GeV and  $M_{A^0} > 88.4$  GeV respectively. But one should note that these constraints on the masses of  $h^0$  and  $A^0$  are not applicable in the 2HDM's because the coupling of  $h^0$  to  $Z^0 Z^0$  and to  $A^0 Z^0$  go like  $\sin \alpha$  and  $\cos \alpha$  ( $\alpha$  is a free parameter of the model), respectively. For a very small mixing angle  $\alpha$  and with  $A^0$  ( $h^0$ ) sufficiently heavy no lower limit on  $M_{h^0}$  ( $M_{A^0}$ ) can be set from the LEP data. For the charged Higgs bosons in the 2HDM's, the 95%*C.L.* limit is  $M_{H^\pm} > 78.6$  GeV [29].

Indirect constraints on Higgs masses come from  $R_b$  and  $\rho$ , which have been measured at LEP. According to studies in Ref. [30], if one requires  $R_b^{theory}$  to be within  $1\sigma$  deviation from  $R_b^{exp}$  and  $\rho$  within  $2\sigma$  deviation from  $\rho^{exp}$ , the preferred range of Higgs boson masses in model III are  $80\text{GeV} < M_{h^0} \simeq M_{A^0} < 120\text{GeV}$  and  $M_{H^\pm} \approx (180 - 220)\text{GeV}$  [30]. On the other hand, if one allows  $R_b^{theory}$  to vary within  $2\sigma$  errors of  $R_b^{exp}$ , a charged Higgs mass of a few hundreds GeV is feasible. In addition, unitary condition requires these masses to be less than  $1\text{TeV}$  [31].

As for the couplings  $\lambda_{ij}^{U,D}$ , a lot of processes have to be analyzed to give reasonable constraints, as have been done in Refs. [18,30]. In Table III, we list current constraints on these couplings along with the processes from which constraints have been or will be placed. It should be noted that despite current constraints on flavor changing couplings  $\lambda_{bs}^D$  and  $\lambda_{tc}^U$  are rather loose, some much more stringent constraints will be imposed in the future experiments.

For simplicity, we set (a) all the FC couplings  $\lambda_{ij}^{U,D} (i \neq j) = 0$ ; (b)  $\lambda_{ii}^U = \lambda_1$  for  $i = u, c, t$ , and  $\lambda_{ii}^D = \lambda_2$  for  $i = d, s, b$ ; and (c)  $\lambda_{1,2}$  are real numbers. The advantage of such a setting is the new contributions to Wilson coefficients discussed below come only from the charged Higgs penguin diagrams and the neutral Higgs bosons are irrelevant to our discussion. The model III therefore differs from the model II only in the couplings of the charged Higgs boson to fermions. The Feynman rules for the  $\bar{U}_i H^+ D_j$  and  $\gamma H^+ H^-$  vertex are

$$\bar{U}_i H^+ D_j : \quad \frac{-i}{2} \left[ V_{CKM} \cdot \xi_{ij}^D (1 + \gamma_5) - \xi_{ij}^U \cdot V_{CKM} (1 - \gamma_5) \right] , \quad (35)$$

$$\gamma H^+ H^- : \quad ie(p_2 - p_1)^\mu , \quad (36)$$

For more details about the couplings between the Higgs bosons and quarks or gauge bosons, one can see Ref. [18].

Another very important source of constraint is the process  $B \rightarrow X_s \gamma$ . In the SM, the theoretical prediction of  $\mathcal{B}(B \rightarrow X_s \gamma)$  is  $(2.8 \pm 0.8) \times 10^{-4}$  at LO approximation [32], and  $(3.28 \pm 0.33) \times 10^{-4}$  at NLO approximation [33]. The 95%*C.L.* limit from CLEO measurement [5] is  $2 \times 10^{-4} < \mathcal{B}(B \rightarrow X_s \gamma) < 4.5 \times 10^{-4}$ . One can see that the theory and the data are in remarkable agreement, which implies that only a narrow parameter space of new physics can survive. Since the aim of this paper is to estimate the new physics effect on the process  $B \rightarrow X_s \gamma \gamma$ , we will vary the input parameters of 2HDM in a rather large range allowed by

$$\frac{2.0 \times 10^{-4}}{2.8 \times 10^{-4}} < \frac{\mathcal{B}_{III}^{LO}(B \rightarrow X_s \gamma)}{\mathcal{B}_{SM}^{LO}(B \rightarrow X_s \gamma)} \Big|_{\mu=m_b} < \frac{4.5 \times 10^{-4}}{2.8 \times 10^{-4}} . \quad (37)$$

### C. Calculation of $B \rightarrow X_s \gamma \gamma$

In model III, the operator bases presented in Eq.(2) are insufficient for the process  $B \rightarrow X_s \gamma \gamma$  and we need following additional operators when all the FC couplings are zero [34]:<sup>3</sup>

$$\begin{aligned}
O_1' &= (\bar{s}_\alpha \gamma^\mu R c_\beta) (\bar{c}_\beta \gamma_\mu R b_\alpha) , \\
O_2' &= (\bar{s}_\alpha \gamma^\mu R c_\alpha) (\bar{c}_\beta \gamma_\mu R b_\beta) , \\
O_{3,5}' &= (\bar{s}_\alpha \gamma^\mu R b_\alpha) \sum_{q=u \cdots b} (\bar{q}_\beta \gamma_\mu (R, L) q_\beta) , \\
O_{4,6}' &= (\bar{s}_\alpha \gamma^\mu R b_\beta) \sum_{q=u \cdots b} (\bar{q}_\beta \gamma_\mu (R, L) q_\alpha) , \\
O_7' &= \frac{e}{16\pi^2} \bar{s}_\alpha \sigma^{\mu\nu} (m_b L + m_s R) b_\alpha F_{\mu\nu} , \\
O_8' &= \frac{g_s}{16\pi^2} \bar{s}_\alpha \sigma^{\mu\nu} (m_b L + m_s R) \lambda_{\alpha\beta}^a b_\beta G_{\mu\nu}^a .
\end{aligned} \tag{38}$$

For the evaluation of Wilson coefficients, we need their initial values with standard matching computations. Denoting the Wilson coefficients in the SM with  $C_i^{SM}(m_W)$  and those from the additional charged Higgs contribution (see Fig.6) with  $C_i^H(m_W)$ , we have the initial values of the Wilson coefficients for the first set of operators [ Eq. (2) ]

$$C_i^{III}(m_W) = C_i^{SM}(m_W) + C_i^H(m_W) , \tag{39}$$

where

$$\begin{aligned}
C_{1 \dots 6}^H(m_W) &= 0 , \\
C_7^H(m_W) &= \frac{1}{2} \left[ \lambda_1^2 f_1(y) + \lambda_1 \lambda_2 f_2(y) + \frac{m_s^2}{m_t^2} \lambda_2^2 f_1(y) \right] , \\
C_8^H(m_W) &= \frac{1}{2} \left[ \lambda_1^2 g_1(y) + \lambda_1 \lambda_2 g_2(y) + \frac{m_s^2}{m_t^2} \lambda_2^2 g_1(y) \right] ,
\end{aligned} \tag{40}$$

and the explicit expressions of  $C_i^{SM}(m_W)$  can be found in the literature [2]. For the primed Wilson coefficients we have

$$C_i'^{III}(m_W) = C_i'^H(m_W) , \tag{41}$$

and  $C_i'^H$  are given as

$$\begin{aligned}
C_{1 \dots 6}'^H(m_W) &= 0 , \\
C_7'^H(m_W) &= \frac{1}{2} \left[ \frac{m_s}{m_t^2} \frac{m_b}{m_t} \lambda_2^2 f_1(y) + \frac{m_s}{m_b} \lambda_1 \lambda_2 f_2(y) + \frac{m_s}{m_b} \lambda_1^2 f_1(y) \right] , \\
C_8'^H(m_W) &= \frac{1}{2} \left[ \frac{m_s}{m_t^2} \frac{m_b}{m_t} \lambda_2^2 g_1(y) + \frac{m_s}{m_b} \lambda_1 \lambda_2 f_2(y) + \frac{m_s}{m_b} \lambda_1^2 g_1(y) \right] .
\end{aligned} \tag{42}$$

---

<sup>3</sup>Here we neglect the operators  $O_{9,10}$  and  $O_{9,10}'$  introduced in [35] because in our case, the corresponding Wilson coefficients keep zero at any scale.

In our calculations we neglect the contributions of the internal  $u$  and  $c$  quarks and define functions  $f_1(y)$ ,  $f_2(y)$ ,  $g_1(y)$ , and  $g_2(y)$  as

$$\begin{aligned} f_1(y) &= \frac{y(7-5y-8y^2)}{72(y-1)^3} + \frac{y^2(3y-2)}{12(y-1)^4} \ln[y] , \\ f_2(y) &= \frac{y(5y-3)}{12(y-1)^2} + \frac{y(-3y+2)}{6(y-1)^3} \ln[y] , \\ g_1(y) &= \frac{y(-y^2+5y+2)}{24(y-1)^3} + \frac{-y^2}{4(y-1)^4} \ln[y] , \\ g_2(y) &= \frac{y(y-3)}{4(y-1)^2} + \frac{y}{2(y-1)^3} \ln[y] , \end{aligned} \quad (43)$$

where  $y = m_t^2/m_{H^\pm}^2$ . Numerical analysis show that  $f_1(y)$  and  $f_2(y)$  have the following properties:

$$f_1(y) < 0, \quad f_2(y) > 0, \quad |f_2(y)| > 3 |f_1(y)| , \quad (44)$$

and  $g_i(y)$  have similar properties.

Using the renormalization group, we can get the LO Wilson coefficients at any scale. The Wilson coefficients  $C_i^{III}(\mu)$  can be obtained from [3] with  $C_i^{SM}(m_W)$  replaced by  $C_i^{III}(m_W)$ , while  $C_i^{\prime III}(\mu)$  are given by<sup>4</sup>

$$\begin{aligned} C_{1\dots 6}^{\prime III}(\mu) &= 0 , \\ C_7^{\prime III}(\mu) &= \eta^{\frac{16}{23}} C_7^{\prime III}(m_W) + \frac{8}{3} (\eta^{\frac{14}{23}} - \eta^{\frac{16}{23}}) C_8^{\prime III}(m_W) , \end{aligned} \quad (45)$$

where  $\eta = \alpha_s(m_W)/\alpha_s(\mu)$ .

The square amplitude summed over spin and polarizations can be written as

$$|A|_{III}^2 = |A|^2 + |A'|^2 + 2|A^* A'| , \quad (46)$$

where the first and second term comes from  $O_1 \sim O_8$  and  $O'_1 \sim O'_8$  respectively and the third term is the interference between them. The explicit expression of  $|A|^2$  is the same as that in Eq.(13) with  $C_i$  being replaced by  $C_i^{III}$ , and  $|A'|^2$  and  $|A^* A'|$  are given by

$$\begin{aligned} |A'|^2 &= \frac{1}{4} \left( \frac{e^2 G_F}{\sqrt{2} \pi^2} V_{tb} V_{ts}^* \right)^2 m_b^4 |F_7'|^2 A_{77} , \\ |A^* A'| &= \frac{1}{4} \left( \frac{e^2 G_F}{\sqrt{2} \pi^2} V_{tb} V_{ts}^* \right)^2 m_b^4 \frac{m_s}{m_b} \{ |F_2^* F_7'| A'_{27} + |F_5^* F_7'| A'_{57} + |F_7^* F_7'| A'_{77} \} , \end{aligned} \quad (47)$$

---

<sup>4</sup>Because the strong interaction preserve chirality, the first set of operators (Eq.(2)) cannot mix with its chirality flipped counterparts, the primed operators, and the anomalous dimension matrices of the two separate set of operators are the same and do not overlap [35]. This means the evaluation of  $C_i'(\mu)$  are the same as in the SM.

where

$$\begin{aligned}
F'_7 &= C_7'^{III} Q_d , \\
A'_{27} &= -2 * s - \frac{(1 + \rho_1)s^2}{t(s-t)} + s * (\rho_1 - \rho) * \left(\frac{1}{t} - \frac{1}{s-t}\right) + (t \leftrightarrow u) , \\
A'_{57} &= Re \left[ 8(\kappa_b + \kappa_s)s - [4(\kappa_b + \rho_1\kappa_s) + 2s(1 - \kappa_b - \kappa_s)] \frac{s^2}{t(s-t)} \right. \\
&\quad \left. + 4(\kappa_b + \kappa_s)(\rho_1 - \rho) \frac{u}{s-t} \right] + (u \leftrightarrow t) , \\
A'_{77} &= 2 * \left[ (1 - \rho)A_{77}^1 + A_{77}^2 \right] - 2s \left( 2 + \frac{2}{t} + \frac{2}{u} + \frac{2(1 - \rho_1 - s)}{tu} \right. \\
&\quad \left. - \frac{(\rho_1 - \rho)(3 + 5\rho_1) - (1 + \rho_1)s}{(s-t)(s-u)} - \frac{(1 - \rho_1)(s^2 + 4\rho_1 tu)}{(s-t)(s-u)tu} \right) . \tag{48}
\end{aligned}$$

In Eq.(47-48),  $m_s$  is the current mass of  $s$  quark and the explicit expressions of  $A_{77}$ ,  $A_{77}^1$  and  $A_{77}^2$  have been given in Eqs.(20-22). For  $|A|_{III}^2$ , two characters should be noted. Firstly, the interference term between  $O_i$  and  $O'_i$  is suppressed by  $m_s/m_b$  and therefore, to a good approximation, can be neglected. Secondly, the total 1PR contributions are proportional to  $(|F_7|^2 + |F'_7|^2)A_{77}$ . Since  $|F_7|^2 + |F'_7|^2$  is not suppressed, as required by  $B \rightarrow X_s \gamma$  in 2HDM [36], the 1PR contribution is then predominant, which is very similar with the case in the SM. As we discussed in section II, these characters mean that the four differential distributions defined in last section cannot have a large deviation from SM predictions and we do not expect to see any new physics signal by the measurement of these four differential distributions. Indeed, we have checked our numerical results in a vast parameter space constrained by Eq.(37), and find it correct.

We are now ready to calculate the new physics corrections to the decay rate of  $B \rightarrow X_s \gamma \gamma$ . In order to reduce the effects of theoretical and experimental uncertainties, we define two ratios

$$R_{\gamma\gamma}(\mu) = \frac{\mathcal{B}_{B \rightarrow X_s \gamma \gamma}^{III}(\mu)}{\mathcal{B}_{B \rightarrow X_s \gamma \gamma}^{SM}(\mu)} , \tag{49}$$

$$R_\gamma(\mu) = \frac{\mathcal{B}_{B \rightarrow X_s \gamma}^{III}(\mu)}{\mathcal{B}_{B \rightarrow X_s \gamma}^{SM}(\mu)} , \tag{50}$$

where the four branching ratios denote the LO theoretical predictions in the SM and model III, respectively.

In the numerical calculation, we consider the following three typical scenarios.

- **Scenario I:**  $|\lambda_1| = |\lambda_2| = \lambda$  and  $m_{H^\pm}$  is about a few hundred GeVs. This scenario can be further divided into two limiting cases:

- Case-1:  $\lambda_1 = \lambda_2 = \lambda$ .
- Case-2:  $\lambda_1 = -\lambda_2 = \lambda$  or  $\lambda_2 = -\lambda_1 = \lambda$ , where  $\lambda$  is positive.

- **Scenario II:**  $\lambda_2 = -2/\lambda_1 = \lambda$  and  $m_{H^\pm}$  is about a few hundred GeVs. By setting <sup>5</sup>  $\lambda = -\sqrt{2} \tan \beta$ , one reproduces the numerical results of the Model II, a very popular version of the two-Higgs-doublet models.
- **Scenario III:**  $|\lambda_2| \gg |\lambda_1|$  and  $m_{H^\pm}$  is about 200 GeV, which is favored by current experiments.

Let us firstly concentrate on Scenario I. From the explicit calculations, we find that the new physics contribution in case-1 tends to increase the value of  $C_7$ . In Figs. 7 and 8, we show the  $\lambda$  dependence of the ratio  $R_{\gamma\gamma}$  in case-1 for fixed  $m_{H^\pm} = 300\text{GeV}$  and assuming  $\mu = 2m_b$  (dashed curve),  $m_b$  (solid curve),  $m_b/2$  (dotted curve), respectively. In determining the range of  $\lambda$ , we have put the constraint of Eq.(37) and required  $C_7$  to be negative and positive respectively.

For the case-1, one can see from Figs. 7 and 8 that

- The  $\mu$  dependence of the ratio  $R_{\gamma\gamma}$  is weak for a negative  $C_7$ : we have  $0.7 \leq R_{\gamma\gamma} \leq 1.0$  within the range of  $1/2 \leq \mu/m_b \leq 2$ .
- The  $\mu$  dependence of the ratio  $R_{\gamma\gamma}$  is strong for a positive  $C_7$ : we have  $0.3 \leq R_{\gamma\gamma} \leq 2.7$  within the range of  $1/2 \leq \mu/m_b \leq 2$ ; which implies that the new physics contribution to the branching ratio  $B \rightarrow X_s \gamma \gamma$  can be significant.
- In the same region of  $\lambda$  as specified in Figs. 7 and 8, the numerical results show that the ratio  $R_{\gamma\gamma}/R_\gamma$  only varies within a very small range of  $1 \pm 0.02$  for  $1/2 \leq \mu/m_b \leq 2$ . This fact reflects the dominance of 1PR contribution to the decay rate of  $B \rightarrow X_s \gamma \gamma$ , and a strong correlation between the branching ratios of  $B \rightarrow X_s \gamma \gamma$  and  $B \rightarrow X_s \gamma$ .

The main feature of case-2 is that the new physics contribution tends to decrease the value of  $C_7$ , as a result, coefficient  $C_7$  keeps negative for all the values of  $\lambda$ . In Fig. 9, we show the dependence of  $R_{\gamma\gamma}$  on  $\lambda$  in case-2 for fixed  $m_{H^\pm} = 300\text{GeV}$  and  $\mu = 2m_b$  (dashed curve),  $m_b$  (solid curve),  $m_b/2$  (dotted curve). It is easy to see that the  $\mu$  dependence of  $R_{\gamma\gamma}$  is weak. Study of the ratio  $R_{\gamma\gamma}/R_\gamma$  gives the same conclusion as in case-1.

In Fig. 10, we plot the  $m_{H^\pm}$  dependence of the ratio  $R_{\gamma\gamma}$  in Scenario I. As one can see from this figure,  $R_{\gamma\gamma}$  tends to approach 1 when the charged-Higgs boson becomes heavier, which is just the decoupling behaviour of the new heavy particle.

Secondly, we consider the Scenario II. By setting  $\lambda = -\sqrt{2} \tan \beta$ , one reproduces the result of the popular model II: the second type of the two-Higgs-doublet models. Wilson coefficient  $C_7$  keeps negative for all the values of  $\lambda$ . In model II, two additional free parameters will enter into our calculation: the charged Higgs mass  $m_{H^\pm}$  and the ratio  $\tan \beta = v_2/v_1$  with  $v_2$  and  $v_1$  are the vacuum expectation value of the two Higgs doublets  $\phi_1$  and  $\phi_2$ .

In Fig.11, we plot the  $\tan \beta$  and  $\mu$  dependences of the ratio  $R_{\gamma\gamma}$  in model II for fixed  $m_{H^\pm} = 500\text{GeV}$ . In this figure, the three curves correspond to  $\mu = 2m_b$  (dashed curve),  $m_b$  (solid curve), and  $m_b/2$  (dotted curve), respectively. One can see that (a) the ratio  $R_{\gamma\gamma}$  is

---

<sup>5</sup>The  $\lambda$  defined in this paper is different from that in Ref. [30] by a factor of  $\sqrt{2}$ .

larger than 1.32 in the whole considered range of  $\tan\beta$  and  $\mu$ , and (b) the ratio  $R_{\gamma\gamma}$  has a weak  $\tan\beta$  dependence for  $\tan\beta \geq 3$ , but sensitive to the variation of scale  $\mu$ .

In Fig.12, we plot the  $\tan\beta$  and  $m_{H^\pm}$  dependences of the ratio  $R_{\gamma\gamma}$  in model II for fixed  $\mu = m_b$ . In this figure, the three curves correspond to  $\tan\beta = 1$  (solid curve), 10 (dashed curve), and 100 (dotted curve), respectively. One can see that the ratio  $R_{\gamma\gamma}$  is insensitive to the variation of  $\tan\beta$ .

Finally, we consider the Scenario III. The main characteristic of this Scenario is that  $C_7$  increases with increasing  $\lambda_1$  for fixed  $\lambda_2$ . In Figs. 13 and 14, we illustrate the  $\lambda_1$  and  $\mu$  dependences of the ratio  $R_{\gamma\gamma}$  for fixed  $m_{H^\pm} = 200$  GeV and  $\lambda_2 = 50$ . In these two figures, the three curves correspond to  $\mu = 2m_b$  (dashed curve),  $m_b$  (solid curve), and  $m_b/2$  (dotted curve), respectively. In determining the range of  $\lambda_1$ , we have considered the constraint of Eq.(37) and required  $C_7$  to be negative and positive for Figs. 13 and 14, respectively. Again, the ratio  $R_{\gamma\gamma}/R_\gamma$  only varies within a very small range of  $1 \pm 0.02$  for  $1/2 \leq \mu/m_b \leq 2$ .

In Fig. 15, we show the  $\lambda_2$  and  $\mu$  dependences of the ratio  $R_{\gamma\gamma}$  for fixed  $m_{H^\pm} = 200$  GeV and  $\lambda_1 = 0.2$ . In this figure, the three curves correspond to  $\mu = 2m_b$  (dashed curve),  $m_b$  (solid curve), and  $m_b/2$  (dotted curve), respectively. In determining the range of  $\lambda_2$ , we have required Eq.(37) to be satisfied. It is easy to see that the ratio  $R_{\gamma\gamma}$  has a strong (moderate) dependence on  $\mu$  ( $\lambda_2$ ). The future NLO calculation of  $R_{\gamma\gamma}$  in the SM and 2HDM's will decrease the  $\mu$  dependence. Study of the ratio  $R_{\gamma\gamma}/R_\gamma$  also shows strong correlations between the branching ratios of  $B \rightarrow X_s\gamma$  and  $B \rightarrow X_s\gamma\gamma$  decays.

In Figs. 16 and 17, we plot  $m_{H^\pm}$ ,  $\lambda_1$  and  $\lambda_2$  dependences of the ratio  $R_{\gamma\gamma}$  in model III and assuming  $\mu = m_b$ . In Fig. 16, the solid and dashed curve refers to  $\lambda_1 = -0.018$  and  $0.010$ , respectively. When choosing the value of  $\lambda_1$ , we keep  $C_7$  to be negative and require  $|C_7| > |C_7^{SM}|$  (solid curve) and  $|C_7| < |C_7^{SM}|$  (dashed curve), respectively. One can find from Fig. 16 that the ratio  $R_{\gamma\gamma}$  tends to approach 1 when charged Higgs boson is becoming heavier. In Fig. 17, the three curves correspond to  $\lambda_1 = 0.2$ ,  $\lambda_2 = 40$  (dashed curve), 50 (solid curve), and 60 (dotted curve), respectively. To determine the range of  $m_{H^\pm}$ , we have required Eq.(37) to be satisfied and  $C_7 > 0$ . Numerical results also show that for a much larger  $m_{H^\pm}$ ,  $C_7$  is driven to be negative.

#### IV. CONCLUSION

In this paper, based on the low-energy effective Hamiltonian, we calculated the rare decay  $B \rightarrow X_s\gamma\gamma$  in the SM and the general two-Higgs-doublet model with the restriction  $\lambda_{ij}^{U,D} = 0$  for  $i \neq j$ . We focused on the estimation of the new physics contributions to the branching ratio  $\mathcal{B}(B \rightarrow X_s\gamma\gamma)$  and the differential distributions  $(1/\Gamma)d\Gamma/ds$ ,  $(1/\Gamma)d\Gamma/d\cos\theta_{\gamma\gamma}$  and  $(1/\Gamma)d\Gamma/dX_\gamma$ .

Within the considered parameter space allowed by currently available data, we found the following:

- In model III, the prediction of the branching ratio  $\mathcal{B}(B \rightarrow X_s\gamma\gamma)$  ranges from one third to three times of the SM prediction, but it is highly correlated with the corresponding theoretical prediction of  $\mathcal{B}(B \rightarrow X_s\gamma)$ .
- In model II, the new physics enhancement to the branching ratio  $\mathcal{B}(B \rightarrow X_s\gamma\gamma)$  can be as large as (30 – 50)% with respect to the SM prediction.

- In the SM and model III, the contribution from 1PR diagrams is dominant and hence those four observable differential distributions are insensitive to the variation of scale  $\mu$  as well as possible new physics corrections considered in this paper.
- Although the process  $B \rightarrow X_s \gamma \gamma$  provides many new physical observables, it is not a better process to detect new physics than  $B \rightarrow X_s \gamma$  because of the smallness of its decay rate and the long-distance background.

At the next-to-leading order, the coefficients of  $O_3 - O_6$  and  $O'_1 - O'_6$  may get enhanced. However, due to their subleading feature, we do not expect drastic deviation from the LO predictions.

### ACKNOWLEDGMENTS

The authors acknowledge the support by the National Natural Science Foundation of China under Grant Nos. 19575015, 19775012 and 10075013, and the Excellent Young Teachers Program of Ministry of Education, P.R.China.

## REFERENCES

- [1] B. Grinstein, R. Springer, and M.B. Wise, Phys. Lett. **B202**,138 (1988); Nucl. Phys. **B339**, 269 (1990); R. Grigjanis, P.J.O. Donnell, M. Sutherland and H. Navelet, Phys. Lett. **B213**, 355 (1998); M. Misiak, Nucl. Phys. **B393**, 23(1993); *ibid*, **B439**, 461(E) (1995); K. Adel and Y.-P. Yao, Mod. Phys. Lett. **A8**, 1679 (1993); Phys. Rev. **D49**, 4945 (1994); M. Ciuchini, E. Franco, G. Martinelli, L. Reina and L. Silvestrini, Phys.Lett. **B316**, 127(1993); Nucl.Phys. **B421**, 41(1994); C. Greub and T. Hurth, Phys.Rev. **D56**, 2934 (1997).
- [2] G. Buchalla, A.J. Buras and M.E. Lautenbacher, Rev. Mod. Phys. **68**, 1125 (1996).
- [3] A.J. Buras and R. Fleischer, in *Heavy Flavours II*, eds. A.J. Buras and M. Lindner (World Scientific, Singapore, 1998), p-65.
- [4] CLEO Collaboration, M.S. Alam *et al.*, Phys. Rev. Lett. **74**, 2885 (1995).
- [5] CLEO Collaboration, S. Ahmed *et al.*, CLEO COF 99-10, hep-ex/9908022.
- [6] K. Chetyrkin, M. Misiak and M. Münz, Phys. Lett. **B400**,206 (1997); Phys. Lett. **B425**, 414(E)(1998); M. Ciuchini, G. Degrassi, P. Gambino and M. Neubert, Nucl. Phys. **B527**, 21(1998); A.K. Kagan and M. Neubert, Eur. Phys. J. **C7**, 5(1999).
- [7] S. Glashow and S. Weinberg, Phy. Rev. **D15**, 1958(1977); J.F. Gunion, H.E. Haber, G. Kane, and S. Dawson, *The Higgs Hunter's Guide*, (Addison-Wesley Publishing Company, 1990); F.M. Borzumati and C. Greub, Phys. Rev. **D58**, 074004 (1998), *ibid*, **D59**, 057501(1999).
- [8] M. Misiak, S. Pokorski, and J. Rosiek, in *Heavy Flavours II*, eds. A.J.Buras and M.Lindner( World Scientific, Singapore, 1998).
- [9] S. Weinberg, Phys. Rev. **D19**, 1277 (1979); L. Susskind, *ibid*, **D20**, 2619 (1979); C.D. Lü, Z.J. Xiao, Phys. Rev. **D53**, 2529 (1996); B. Balaji, Phys. Rev. **D53**, 1699 (1996); G.R. Lu, Z.H. Xiong and Y.G. Cao, Nucl. Phys. **B487**, 43 (1997); Z.J. Xiao *et al.*, Chin. Phys. Lett. **16**, 88 (1999); Z.J. Xiao *et al.*, Eur. Phys. J. **C7**, 487 (1999); Z.J. Xiao *et al.*, Commun. Theor. Phys. **33**, 269 (2000).
- [10] M.R. Ahmady, E. Kou and A. Sugamoto, Phys. Rev. **D57**, 1997 (1998).
- [11] G.-L. Lin, J. Liu and Y.-P. Yao, Phys. Rev. Lett. **64**, 1498 (1990); Phys. Rev. **D42**, 2314 (1990); H. Simma and D. Wyler, Nucl. Phys. **B44**, 283 (1990); S. Herrlich and J. Kalinowski, Nucl. Phys. **B381**, 501 (1992).
- [12] L. Reina, G. Ricciardi, and A. Soni, Phys. Lett. **B396**, 231 (1997).
- [13] C.-H.V. Chang, G.-L. Lin, and Y.-P. Yao, Phys. Lett. **B415**, 395 (1997).
- [14] L. Reina, G. Ricciardi, and A. Soni, Phys. Rev. **D56**, 5805 (1997).
- [15] J. Chay *et al.*, Phys. Lett. **B247**, 399 (1990); A.F. Falk, M. Luke, and M.J. Savage, Phys. Rev. **D49**, 3367 (1994).
- [16] S.Rai Choudhury and York-Peng Yao, Phys. Rev. **D58**, 034011 (1998).
- [17] T.P. Cheng and M. Sher, Phys.Rev. **D35**, 3484 (1987); M. Sher and Y. Yuan, Phys.Rev. **D44**, 1461 (1991); W.S. Hou, Phys.Lett. **B296**, 179 (1992); A. Antaramian, L.J. Hall, and A. Rasin, Phys. Rev. Lett. **69**, 1871 (1992); L.J. Hall and S. Weinberg, Phys.Rev. **D48**, R979 (1993); D. Chang, W.S. Hou, and W.Y. Keung, Phy.Rev. **D48**, 217 (1993); Y.L. Wu and L. Wolfenstein, Phys.Rev.Lett. **73**, 1762 (1994); D. Atwood, L. Reina, and A. Soni, Phy.Rev. Lett. **75**, 3800 (1995); G. Cvetcic, S.S. Hwang, and C.S. Kim, Phys.Rev. **D58**, 116003 (1998).



- [18] D. Atwood, L. Reina, and A. Soni, Phys. Rev. **D55**, 3156 (1997); *ibid*, **D 54**, 3296 (1996).
- [19] Z.J. Xiao, C.S. Li, and K.T. Chao, Phys. Lett. **B473**, 148 (2000); Z.J. Xiao, C.S. Li, and K.T. Chao, Phys. Rev. **D62**, 094008 (2000); Z.J. Xiao, C.S. Li, and K.T. Chao, Phys. Rev. **D63**, 074005 (2001);
- [20] G.-L. Lin, J. Liu, and Y.-P. Yao, Phys. Rev. Lett. **64**, 1498 (1990); Phys. Rev. **D42**, 2314 (1990); F.E. Low, Phys. Rev. **110**, 974 (1958).
- [21] B. Grinstein, R. Springer, and M.B. Wise, Nucl. Phys. **B339**, 269 (1990); H. Simma, Z.Phys. **C61**, 67 (1994).
- [22] M. Ciuchini, E. Franco, G. Martinelli, L. Reina, and L. Silvestrini, Phys. Lett. **B316**, 127 (1993); Nucl. Phys. **B421**, 41 (1994); A.J. Buras, M. Misiak, M. Münz, and S. Pokorski, *ibid*. **B424**, 374 (1994).
- [23] A. Ali and C. Greub, Phys. Lett. **B259**, 182 (1991); Z.Phys. **C49**, 421 (1991); Phys. Lett **B361**, 146 (1995).
- [24] For more details, see for example, R.D. Field, *Applications of perturbative QCD*, (Addison-Wesley, 1989).
- [25] S. Bertolini and J. Matias, Phys. Rev. **D57**, 4197 (1998).
- [26] M. Kobayashi and T. Maskawa, Prog. Theor. Phys. **49**, 652 (1973).
- [27] For more details about the experimental constraints on Higgs bosons, one can see, *Review of Particle Physics*, D.E. Groom *et al.*, Eur. Phys. J. **C15**, 1 (2000), and references therein.
- [28] P.Igo-Kemenes, for the LEP Working Group on Higgs boson searches, talk at the LEPC open session on Nov. 3rd, 2000.
- [29] LEP Higgs working group, CERN-EP-2000-055, prepared from contributions of the LEP experiments to the Winter 2000 Conference.
- [30] David Bowser-Chao, K. Cheung, and W.-Y. Keung, Phys. Rev. **D59**, 115006 (1999).
- [31] M. Veltman, Phys. Lett. **B70**, 253 (1977); B.W. Lee, C. Quigg, H.B. Thacker, Phys. Rev. **D16**, 253 (1977).
- [32] A.J. Buras, M. Misiak, M. Münz and S. Pokorski, Nucl. Phys. **B424**, 374 (1994); W.S. Hou and R.S. Willey, Phys. Lett. **B202**, 59 (1988); S. Bertolini, *et al.*, Nucl. Phys. **B353**, 591 (1991); C.D. Lü, Nucl. Phys. **B441**, 33 (1994).
- [33] C. Greub, T. Hurth, and D. Wyler, Phys. Lett. **B380**, 385 (1996); Phys. Rev. **D54**, 3350 (1996); K.G. Chetyrkin, M. Misiak and M. Münz, Phys. Lett. **B400**, 206 (1997); *ibid*, **B425**, 414(E)(1998).
- [34] T.M. Aliev and E.O. Iltan, Phys. Rev. **D58**, 095014 (1998).
- [35] P. Cho and M. Misiak, Phys. Rev. **D49**, 5894 (1994).
- [36] T.M. Aliev and E.O. Iltan, J. Phys. **G25**, 989 (1999).

# TABLES

TABLE I. Values of the regularization-scheme-independent LO Wilson coefficients  $C_i(\mu)$  using the input parameters as listed in Table II.

| $\mu$   | $C_1$  | $C_2$ | $C_3$ | $C_4$  | $C_5$ | $C_6$  | $C_7$  |
|---------|--------|-------|-------|--------|-------|--------|--------|
| $m_b/2$ | -0.315 | 1.143 | 0.015 | -0.032 | 0.009 | -0.041 | -0.340 |
| $m_b$   | -0.225 | 1.10  | 0.010 | -0.023 | 0.007 | -0.028 | -0.304 |
| $2m_b$  | -0.154 | 1.061 | 0.007 | -0.016 | 0.005 | -0.019 | -0.273 |

TABLE II. Values of the input parameters used in the numerical calculations.

| $\alpha_s(m_Z)$       | $\alpha_e$ | $m_t$  | $m_Z$   | $m_W$               | $m_b$      | $m_c$                                    |
|-----------------------|------------|--------|---------|---------------------|------------|--|
| 0.118                 | 1/129      | 175GeV | 91.2GeV | 80.4GeV             | 4.8GeV     | 1.5GeV                                   |
| $m_s(\text{current})$ | $m_K$      | $m_u$  | $m_d$   | $ V_{ts}^* V_{tb} $ | $ V_{bc} $ | $\mathcal{B}(b \rightarrow X_c e \nu_e)$ |
| 0.15GeV               | 0.5GeV     | 5.1MeV | 9.0MeV  | 0.04                | 0.04       | 0.11                                     |

TABLE III. Current constraints on  $\lambda_{ij}^{U,D}$  along with the processes from which constraints have been or will be placed. Couplings that do not appear in this table are not constrained.

| coupling         | current constrain | current constrain from                    | future constrain from  |
|------------------|-------------------|---|--|
| $\lambda_{sd}^D$ | $\ll 1$           | $K^0 - \bar{K}^0$ mixing                  |  |
| $\lambda_{bd}^D$ | $\ll 1$           | $B_d - \bar{B}_d^0$ mixing                |  |
| $\lambda_{uc}^U$ | $\ll 1$           | $D^0 - \bar{D}^0$ mixing                  |  |
| $\lambda_{tt}^U$ | $< 0.5$           | $R_b, B_d - \bar{B}_d^0$ mixing           |  |
| $\lambda_{bb}^D$ | $\geq 40$         | $R_b, R_c$                                |  |
| $\lambda_{sb}^D$ | $\leq 40$         | $b \rightarrow scc$ and $B_s - \bar{B}_s$ | $Z \rightarrow bs, B_{d,s}^0 \rightarrow l^+ l^-, b \rightarrow X_s \mu^+ \mu^-$ |
| $\lambda_{tc}^u$ | -                 | -   | $e^+ e^- \rightarrow tc, t \rightarrow c\gamma, cZ, cg$                          |

# FIGURES

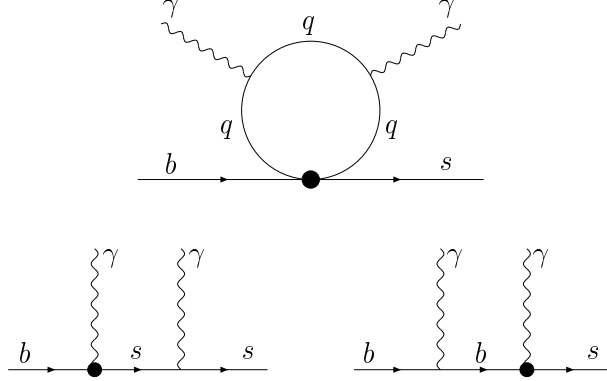


FIG. 1. Examples of Feynman diagrams that contribute to the matrix elements  $\langle s\gamma\gamma | H_{eff} | b \rangle$ . The 1PI diagrams illustrate possible insertion of  $O_1 \sim O_6$ , while the 1PR diagrams represent the insertion of  $O_7$ .

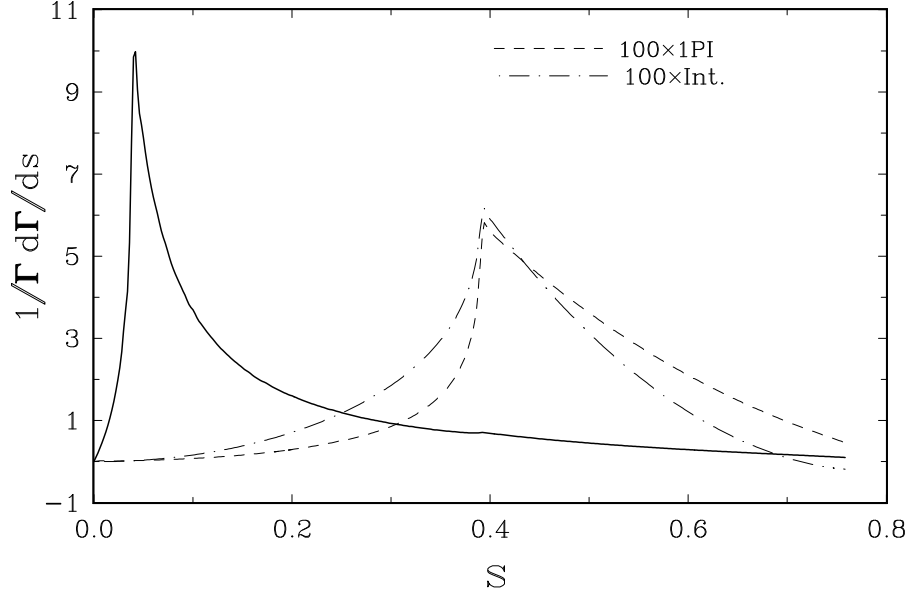


FIG. 2. The normalized distribution  $1/\Gamma d\Gamma/ds$  versus  $s$  in the SM (solid line). The contribution from 1PI diagrams (dashed line) and that from the interference between 1PI and 1PR diagrams (dot dashed line) are also shown. In plotting this diagram, we set  $\mu = m_b$ . The mean value of  $s$  is 0.18 for the cuts as given in the text.

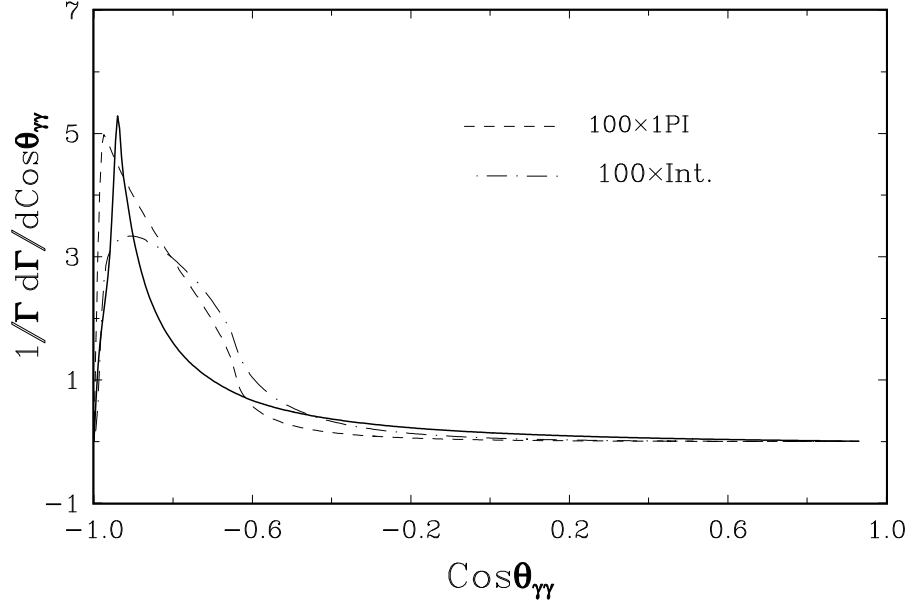


FIG. 3. The normalized distribution  $1/\Gamma d\Gamma/d(\cos \theta_{\gamma\gamma})$  versus  $\cos \theta_{\gamma\gamma}$  in the SM (solid curve) for fixed  $\mu = m_b$ . The contribution from 1PI diagrams (dashed curve) and the interference between 1PI and 1PR diagrams (dot-dashed curve) are also plotted. The mean value of  $\cos \theta_{\gamma\gamma}$  is -0.70 for the cuts as given in the text.

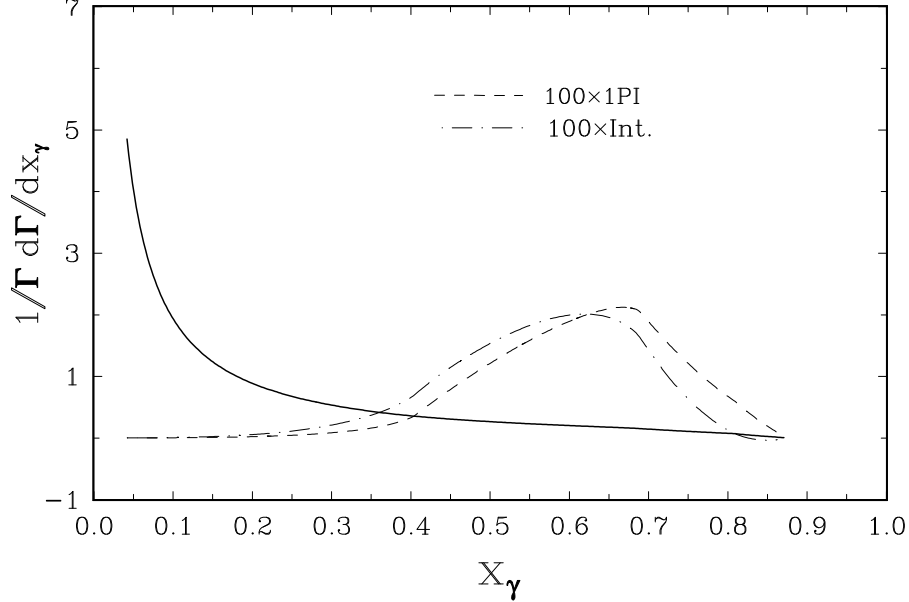


FIG. 4. The spectra of lower energy photons (solid curve) in the SM. The contribution from 1PI diagrams (dashed curve) and that from the interference between 1PI and 1PR diagrams (dot-dashed curve) are also shown. In plotting this diagram, we set  $\mu = m_b$ ,  $X_\gamma = 2E_\gamma/m_b$  and normalize the spectra to the total QCD corrected rate.

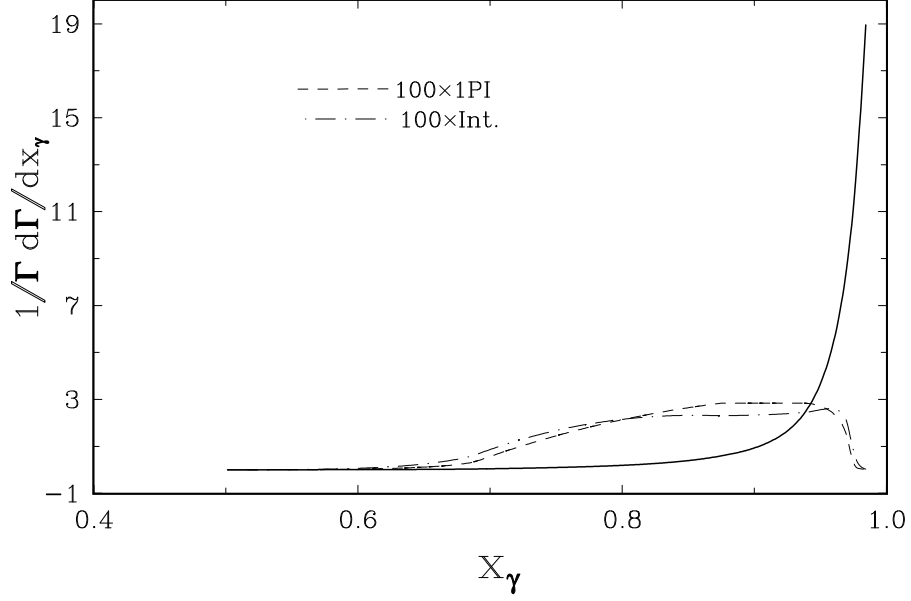


FIG. 5. Same as Fig.4, but for the spectrum of high energy photon.

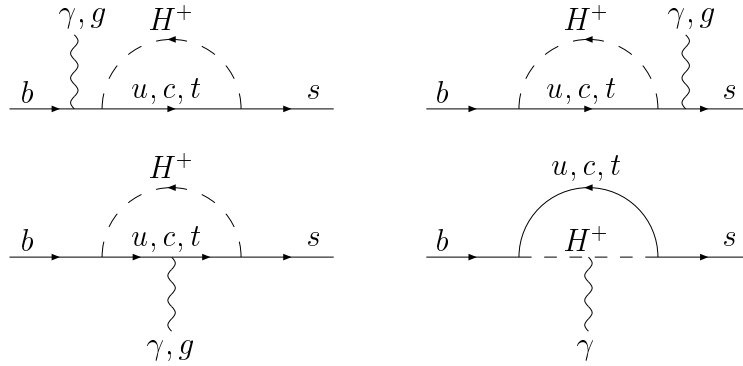


FIG. 6. The Feynman diagrams relevant to the decays  $b \rightarrow s\gamma$  and  $b \rightarrow sg$  in model III. From these diagrams,  $C_i^H$  and  $C_i'^H$  can be extracted. The internal quarks are the upper type  $u$ ,  $c$  and  $t$  quarks.

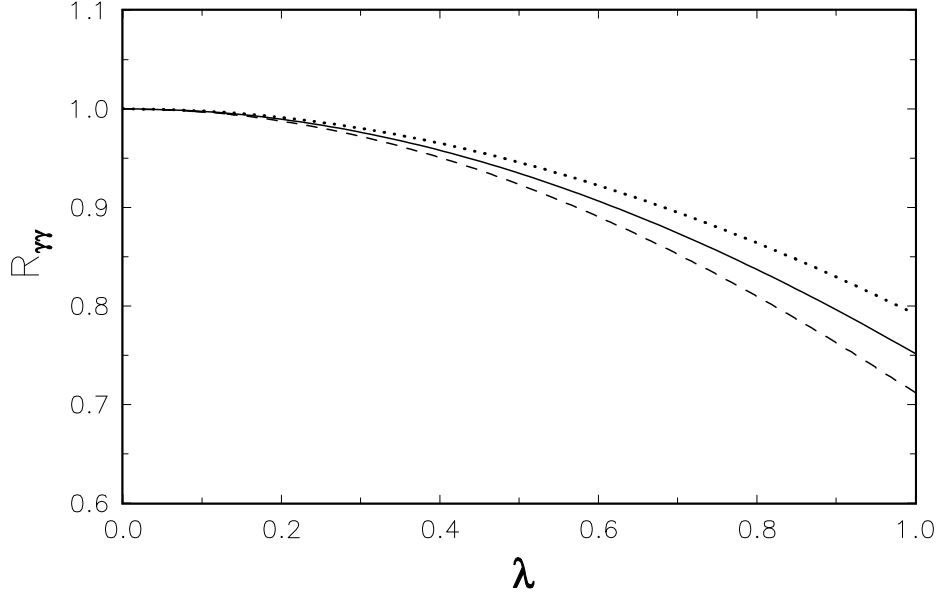


FIG. 7.  $R_{\gamma\gamma}$  as a function of the coupling  $\lambda$  in the Case-1 of Scenario I for fixed  $m_{H^\pm} = 300\text{GeV}$ . The dashed, solid and dotted curve correspond to  $\mu = 2m_b$ ,  $m_b$  and  $m_b/2$ , respectively. In determining the range of  $\lambda$ , we have required Eq.(37) to be satisfied and  $C_7$  to be negative.

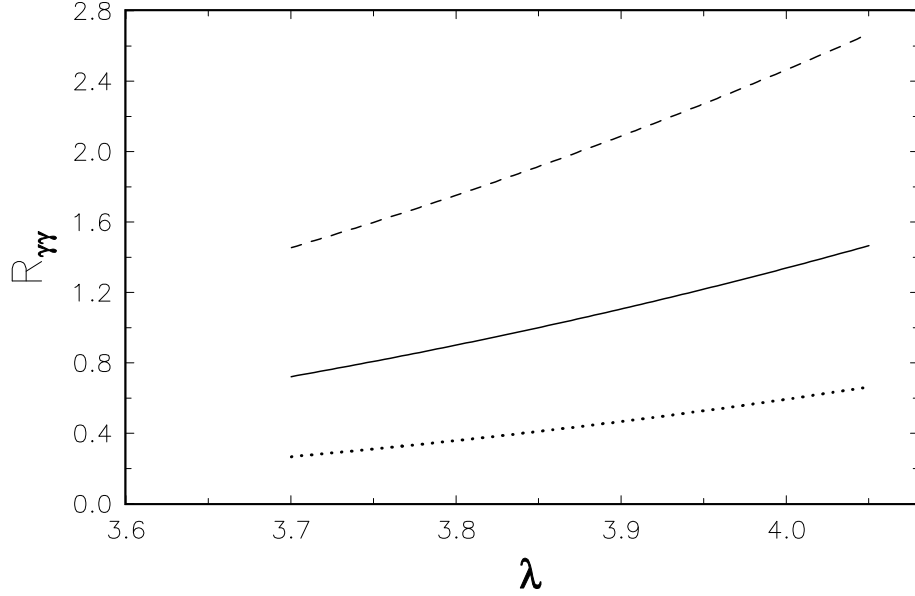


FIG. 8. Same as Fig.7, but for a positive  $C_7$ .

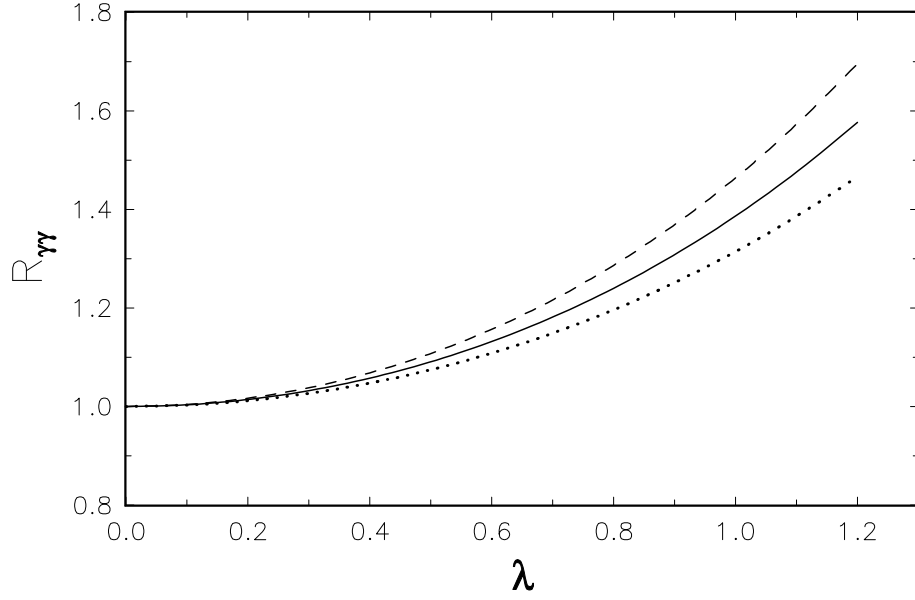


FIG. 9. Same as Fig.7, but for the Case-2 of Scenario I. In this case,  $C_7$  keeps negative for all the values of  $\lambda$ .

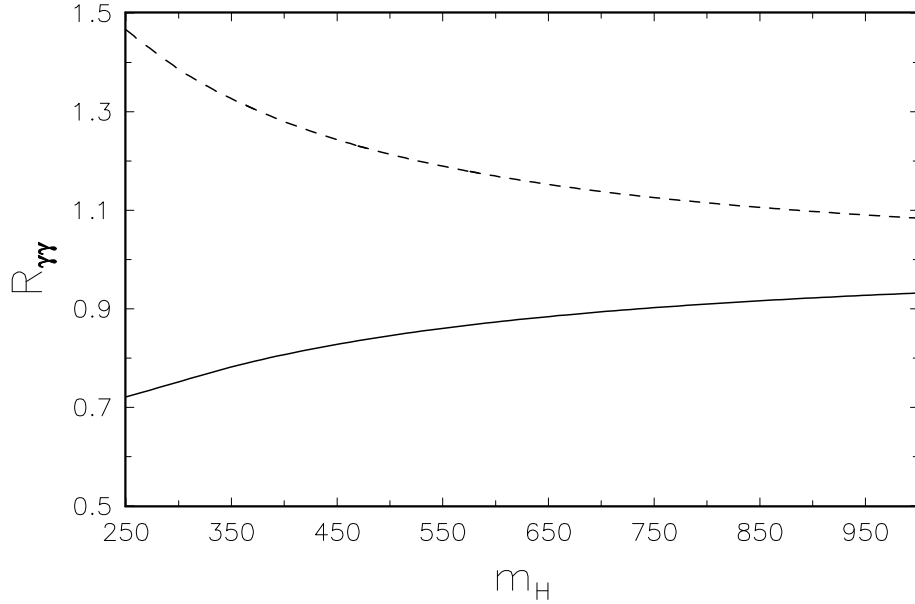


FIG. 10. The dependence of  $R_{\gamma\gamma}$  on the charged Higgs mass  $m_{H^\pm}$  for Case-1 (solid curve) and Case-2 (dashed curve) in scenario I. In either case,  $C_7$  is negative and we set  $\lambda = 1$  and  $\mu = m_b$ .

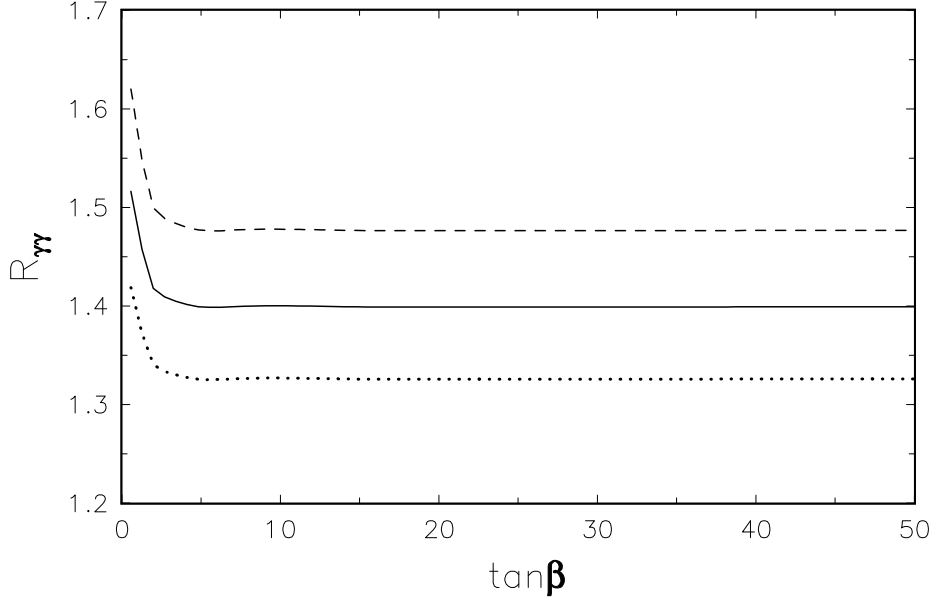


FIG. 11.  $\tan\beta$  and  $\mu$  dependences of the ratio  $R_{\gamma\gamma}$  in model II for fixed  $m_{H^\pm} = 500$  GeV. The dashed, solid and dotted curves correspond to  $\mu = 2m_b$ ,  $m_b$ , and  $m_b/2$ , respectively. In numerical calculation, we have required the constraints as given in Eq.(37) to be satisfied.

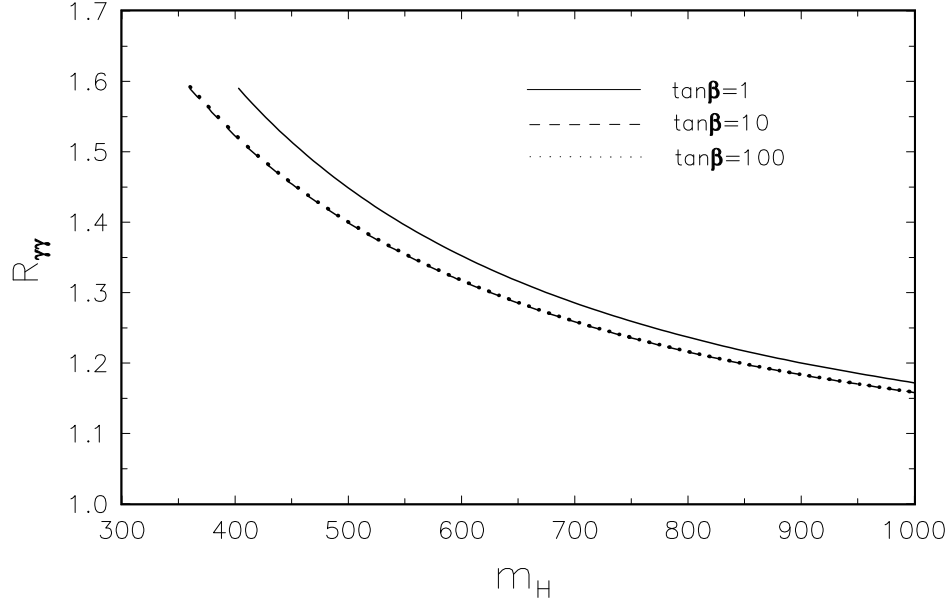


FIG. 12.  $m_{H^\pm}$  and  $\tan\beta$  dependences of  $R_{\gamma\gamma}$  in model II for fixed  $\mu = m_b$ . The solid, dashed and dotted curves correspond to  $\tan\beta = 1, 10, 100$ , respectively. The last two curves can not be separated clearly. In numerical calculation, we have required the constraints as given in Eq.(37) to be satisfied.



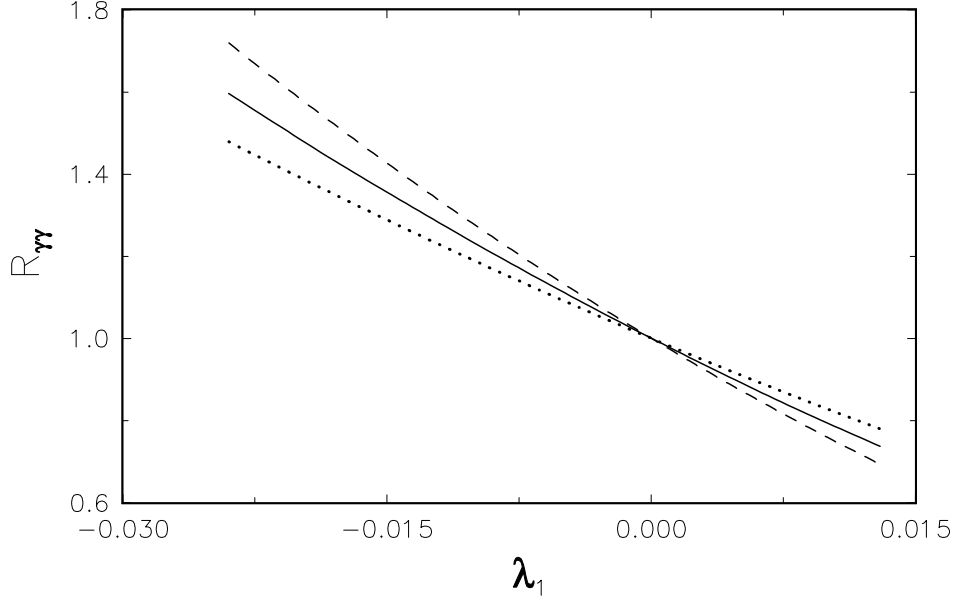


FIG. 13. The dependence of  $R_{\gamma\gamma}$  on  $\lambda_1$  in scenario III for fixed  $\lambda_2 = 50$  and  $m_{H^\pm} = 200\text{GeV}$ . The dashed, solid and dotted curves corresponds to  $\mu = 2m_b$ ,  $m_b$  and  $m_b/2$  respectively. In determining the range of  $\lambda_1$ , we required Eq.(37) to be satisfied and  $C_7$  to be negative.

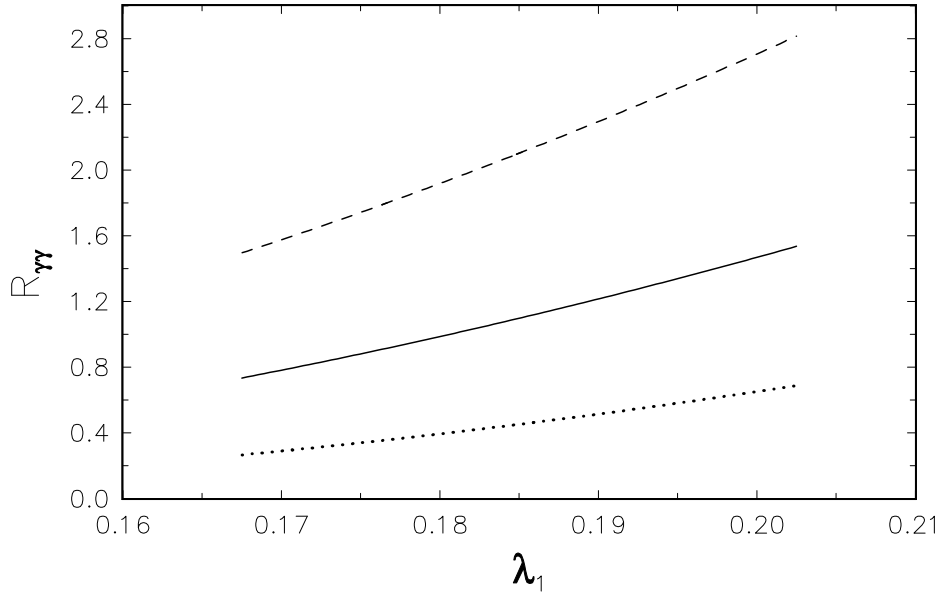


FIG. 14. Same as Fig.13, but for a positive  $C_7$ .

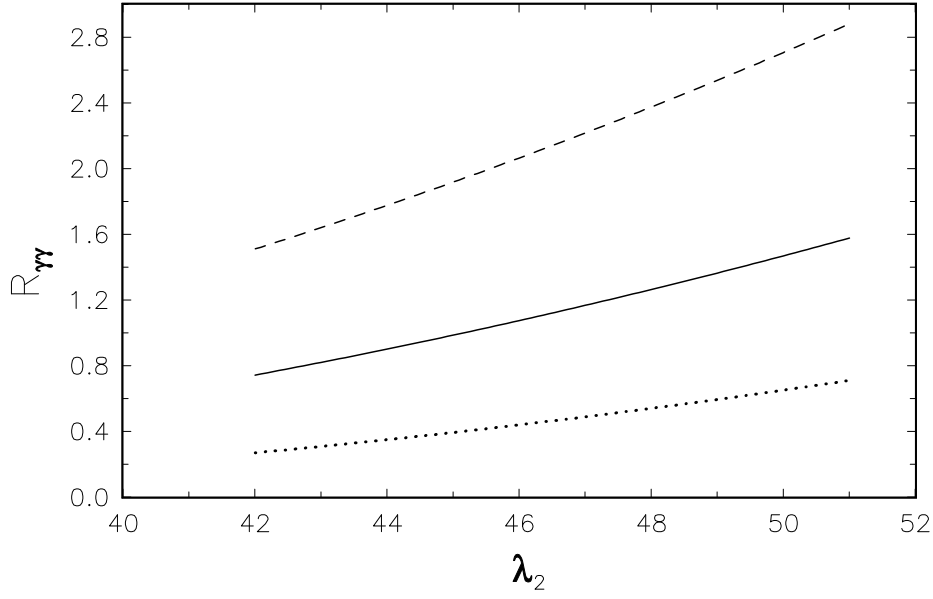


FIG. 15. The relationship between  $R_{\gamma\gamma}$  and  $\lambda_2$  in scenario III for fixed  $\lambda_1 = 0.2$  and  $m_{H^\pm} = 200\text{GeV}$ . The dashed, solid and dotted curves corresponds to  $\mu = 2m_b$ ,  $m_b$  and  $m_b/2$  respectively. In determining the range of  $\lambda_2$ , we have required Eq.(37) to be satisfied and  $\lambda_2 \gg \lambda_1$ .

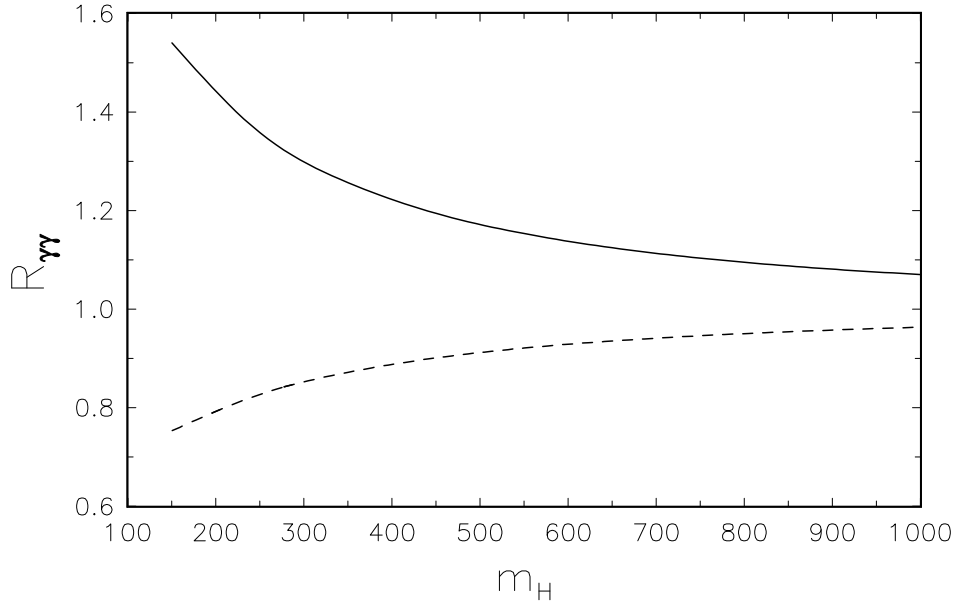


FIG. 16.  $R_{\gamma\gamma}$  as a function of the charged Higgs mass  $m_{H^\pm}$  for  $\lambda_2 = 50$  and  $\mu = m_b$ . Solid and dashed curve correspond to  $\lambda_1 = -0.018$  and  $0.010$ , respectively. When choosing the value of  $\lambda_1$ , we keep  $C_7$  to be negative and require  $|C_7| > |C_7^{SM}|$  (solid curve) and  $|C_7| < |C_7^{SM}|$  (dashed curve), respectively.

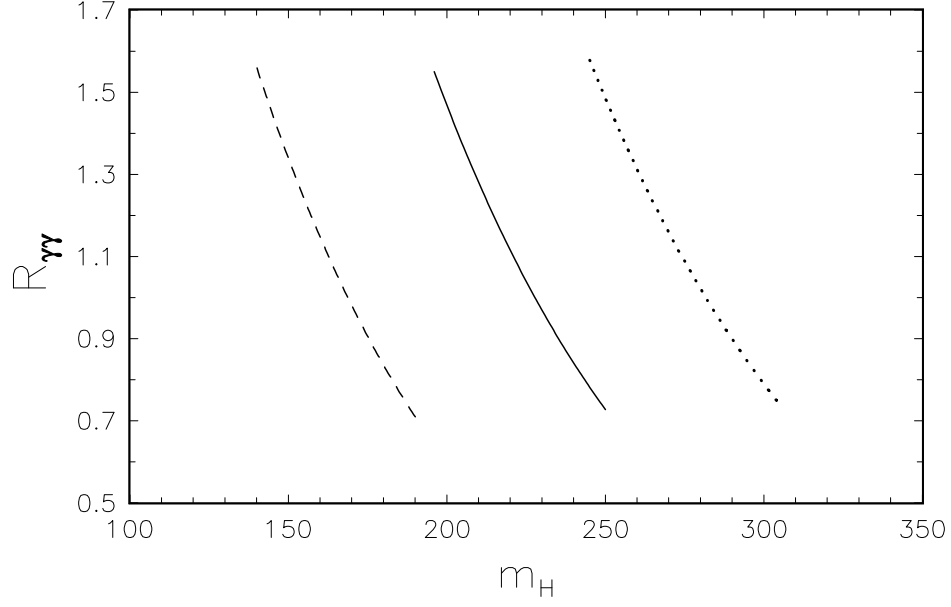


FIG. 17.  $m_{H^\pm}$  dependence of  $R_{\gamma\gamma}$  for fixed  $\lambda_1 = 0.2$ ,  $\mu = m_b$  and  $\lambda_2 = 40$  (dashed curve), 50 (solid curve), 60 (dotted curve). To determine the range of  $m_{H^\pm}$ , we require Eq.(37) to be satisfied and  $C_7 > 0$ . Numerical results also show that for a large  $m_{H^\pm}$ ,  $C_7$  is driven to be negative.